Correlational Analysis of Proteins and Nonmetallic Nanoparticles in a Deep-Nulling Microscope

Michael Hilbert,[†] Hendrik Hippchen,[†] Axel Wehling,[‡] and Peter J. Walla*,[†,‡]

Max-Planck-Institute for Biophysical Chemistry, Department 010, Spectroscopy and Photochemical Kinetics, Am Fassberg 11, D-37077 Göttingen, Germany, and Technical University of Brunswick, Institute for Physical and Theoretical Chemistry, Department for Biophysical Chemistry, Hans-Sommerstr. 10, D-38106 Braunschweig, Germany

We present a method for label-free microscopic analysis of nonmetallic nanoparticles such as biopolymers or technical polymers diffusing freely in an aqueous environment. We demonstrate the principal feasibility of the approach with first measurements of 20−200 nm sized polystyrene spheres and of the ∼10 nm protein complex Photosystem I (PS I) of *Thermosynechococcus elongatus*. The approach is based on the combination of a microscope setup with a deep-nulling interferometer for measuring minute refractive index changes or absorptions in the focal area of the microscope. It is possible to obtain transient nulls in a microscope setup on the order of 10^{-5}, corresponding to optical pathway differences of less than 0.6 nm and to stabilize the nulls to about $5 \cdot 10^{-4}$. With this level of stabilization it is possible to perform a fast (1 s) correlational analysis of aqueous solutions containing the protein complex PS I or 20 nm spheres and to detect in real time single diffusional transits of larger nanospheres through the focal area of the microscope. A modulated heating of the samples in the microscope focus is not necessary for detection. The interferometer correlation data correspond well to conventional two-photon excited fluorescence correlation (FCS) data measured in the same setup, providing evidence that the detection volumes are of a similar size (∼200 nm). We also conducted first nulling experiments using coherent near-field sources of about 30 nm diameter. Theoretical considerations indicate that this combination with nanometric near-field sources will even allow label-free single-protein analysis.

Introduction

Methods based on fluorescence microscopy are a very important tool for investigating biomolecular mechanisms and have been used for several decades now.[1] The ultimate sensitivity of fluorescence techniques was reached when, in 1990, M. Orrit for the first time showed the principal feasibility of optical single-molecule detection based on fluorescence excitation spectroscopy. These findings opened a completely new field, with applications ranging from research on the most basic principles of molecular photophysics to exploration of biomolecular mechanisms in real time at the single biomolecule level.[2−9] Important examples of biomolecular mechanisms, for which evidence could be provided on a single biomolecule level only, are: the rotational mechanism of ATPase[10] or the motility mechanism of myosin moving along actin.[11] Optical techniques such as fluorescence correlation spectroscopy (FCS), fluorescence lifetime measurements, fluorescence resonance energy transfer (FRET), and two-photon excitation (TPE) on a single molecular level, to name only a few, are well-established nowadays.[12−16]

However, all techniques mentioned require labeling of at least one reaction partner or the biomolecules of interest, which represents a severe drawback. Besides the influence of the labeling on the investigated biomolecular mechanism, the labeling procedure itself is, in most cases, complicated and subject to errors. Moreover, each system requires a different labeling approach.

It is for these reasons that researchers deeply wish to have label-free detection technologies, a wish that resulted in the development of techniques such as surface plasmon resonance measurements (SPR).[17,18] SPR measures minute changes in the refractive index at surfaces that are covered with biomolecules such as antibodies. The method allows, for example, to measure binding of additional antibodies on the nanometer scale. The principle is very well established, but still, one reaction partner has to be attached chemically or physically to the surface of the device. This has an impact on the biochemistry, which is probably not less severe than labeling simply with a fluorescent dye. Furthermore, many applications do not allow measurements at a surface or they require freely diffusing reaction partners, let alone measurements in whole cells. Among other appealing approaches, such as coherent anti-Stokes Raman scattering (CARS) microscopy,[19,20] is photothermal interference contrast.[21−24] The advantage of interference contrast methods over scattering methods is that they are more sensitive for detecting smaller particles. Scattering methods decay with the sixth power of the particle diameter, whereas thermal interference contrast methods decrease only with the third power of the diameter. The approach visualizes the change of the refractive index due to a modulated heating of larger nonmetallic spheres[21] or metallic nanoparticles[23] with a very high contrast using the principles of differential interference contrast microscopy. This method allows an unambiguous detection of metallic nanoparticles down to

* Author to whom correspondence should be addressed. E-mail: pwalla@gwdg.de.
† Max-Planck-Institute for Biophysical Chemistry.
‡ Technical University of Brunswick.

Proteins and Nanoparticles in a Deep Nulling Microscope

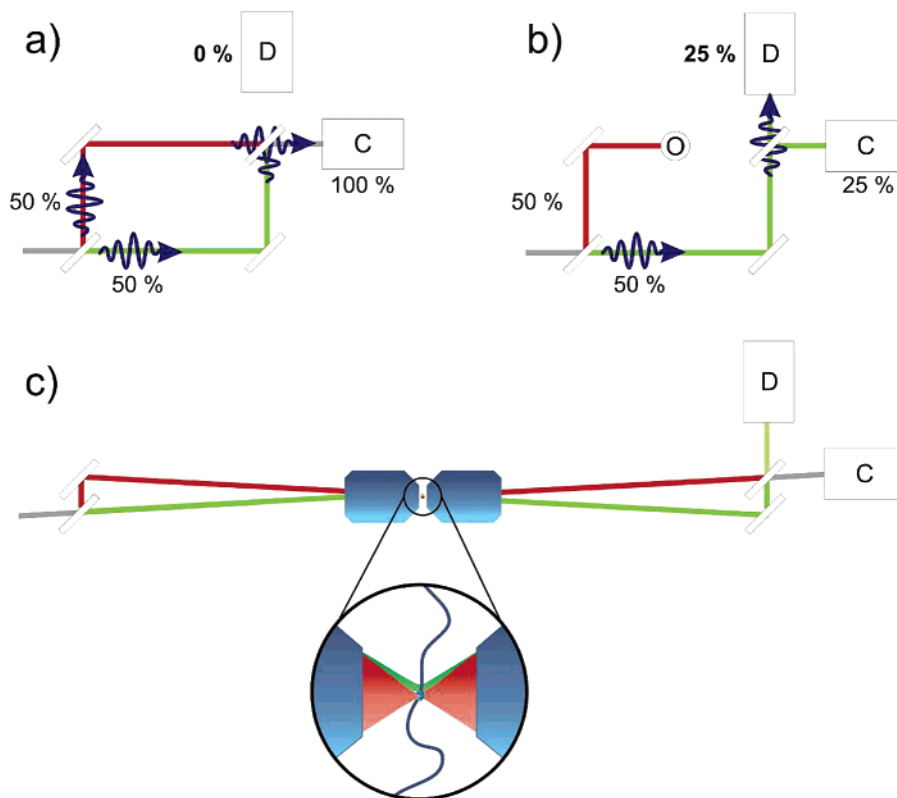*J. Phys. Chem. B, Vol. 109, No. 38, 2005* **18163**

Figure 1. Basic principle of the nulling experiment.

67 atoms in size, even in strongly scattering samples. However, the samples are heated to about 15 K above the average ambient temperature, which might be too high for some proteins or other biomolecules.

In this report, we present first results of an approach using deep-nulling interferometry in a microscope setup. This approach enables a label-free microscopic detection and correlational analysis of nonmetallic (bio)polymers diffusing freely in an aqueous environment without heating[21] of the samples.

Basic Principle

The scheme of the approach is simple: Figure 1a shows a standard Mach−Zender interferometer with a nulled dark exit (D) and a constructively interfering bright exit (C) with corresponding detectors.[25,26] Without any disturbance, no photon is detected at the dark exit in a perfect interferometer.

Because of the wave/particle nature of light, this is still true when single photons are sent into the interferometer − the photons are interfering with themselves and, therefore, always exiting at the bright exit (C) of the interferometer (Figure 1a). However, an object, e.g., a biomolecule, disturbing the coherence in one arm of the interferometer will be indicated directly by photons detected at the dark exit (D). Interestingly, even a single photon, which travels along the undisturbed arm of the interferometer, can then be detected at the dark exit, providing interaction-free evidence that there is an object in the other arm (Figure 1b).[25] Because each single photon is destructively interfering with itself, it is possible to measure signals that are smaller than the shot noise of the measuring light field. The scheme can easily be combined with a pair of microscope objectives (Figure 1c). The two interferometric arms can be sent into the microscope objectives with a small angle, which results in two spatially separated foci. For a perfectly nulled interferometer, even the smallest disturbance of the coherence in one of the foci due to refractive index fluctuations, absorptions, or

nonlinear effects such as the optical Kerr effect will directly be indicated by photons detected at the otherwise absolutely dark exit (D). Fluctuations in regions more remote to the focal region contribute a lot less because they have basically the same effect on both arms of the interferometer. This feature is similar to the sectioning capability of differential interference contrast (DIC) microscopy for complex objects such as cells. In practice, the sensitivity of the approach depends on the residual photon count number at the dark exit and, therefore, the nulling depth. For a correlational analysis of the fluctuating signals, a deep null is also advantageous because artificial correlation signals caused by light source fluctuations can be canceled out. In addition, we do not need a modulation of the signals for lock-in amplification that would interfere with the correlational analysis.

Practical Implementation

The practical application of this approach depends very much on the ability to deeply null light using a microscope and aqueous solutions. To our knowledge, the best nulls in a tabletop setup reported in the literature were achieved by astronomers for the cancellation of star light to detect light from planets nearby.[27−29] Besides a special geometrical design, these nulls were achieved by actively controlling the optical path length difference, x_{OPD}, using a piezotransducer attached to a mirror of one interferometer arm. When all optical elements are perfect, the nulling depth, D, as function of the optical pathway difference, x_{OPD}, is

$$D = \frac{N}{N_0} = \cos^2\frac{\phi}{2} = \cos^2\frac{x_{OPD}\pi}{\lambda} \approx \left(\frac{x_{OPD}\pi}{\lambda}\right)^2 \text{ for small } x_{OPD}$$

(1)

Here, N_0 is the number of incident photons, N, the number of photons at the dark exit (D), λ, the wavelength of the incident
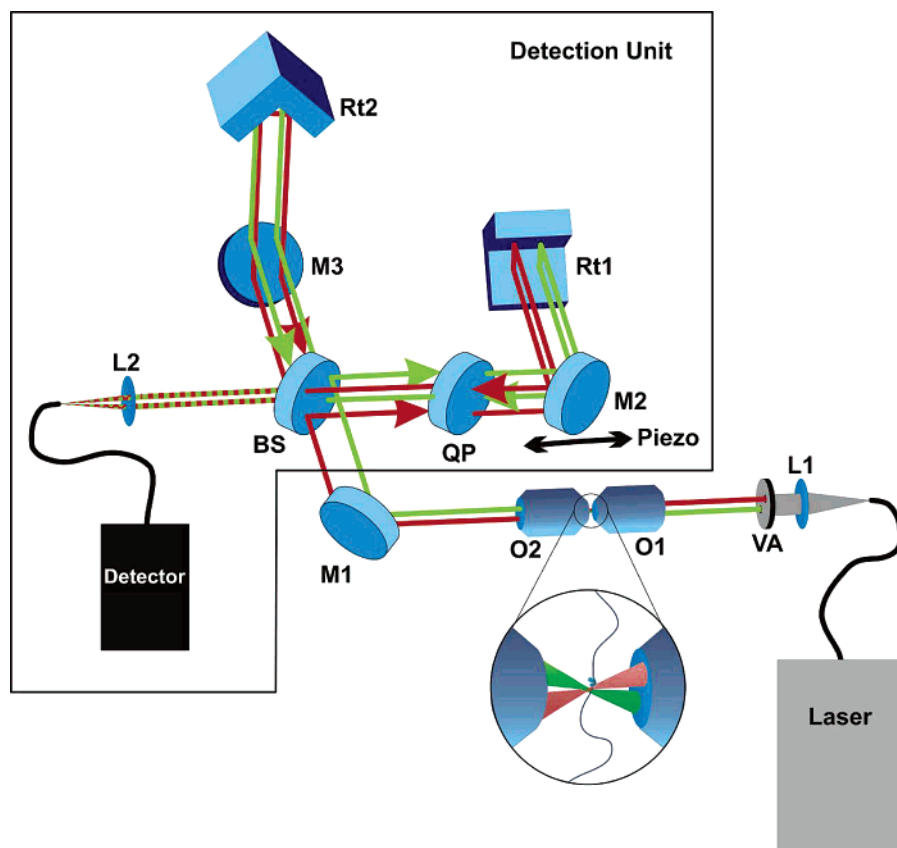
Figure 2. Schematic representation of the experimental setup. Two quadrants of the original beam (grey before the virtual aperture VA) are canceled out with each other in the detection unit. They are shown as red and green lines after VA for better visibility. The interferometer is deduced from ref 28. For details, see text.

light, and $\phi = x_{OPD}\pi$, the phase error. In the tabletop setup reported in ref 27, a null of 10^{-5} was realized with spectrally broad white light. Such a null corresponds to $x_{OPD} \approx 0.5$ nm, a length scale well below typical protein diameters.

For a microscopic application of the interferometer described in refs 27 and 28, we inserted two additional microscope objectives (Figure 2).

As light source, the tip of a monomode fiber is used, which represents a virtually ideal coherent point source and allows switching between different light sources. The light emerging from the fiber tip (indicated with gray color) is first collimated using the lens L1 ($f = 5$ cm). The design of the deep nulling interferometer is such that diagonal quadrants of this originally collimated beam are canceled with each other. This is realized in the part of the interferometer that is denoted as the detection unit in Figure 2. The two roof-top mirrors Rt1 and Rt2 superimpose pair-wise diagonal quadrants of the incoming beam onto each other for detection (after L2). Two such diagonal quadrants and their optical paths are indicated using red and green lines in Figure 2. Note that actually, four quadrants are present, but only two are shown in Figure 2. For better visibility a virtual aperture (VA) is sketched in Figure 2, which selects the two diagonal quadrants. However, in the real setup, such an aperture is not necessary. The beam quadrants, which are part of the incoming single beam, are focused and collimated by the two objectives O1 and O2. The sample itself is located between O1 and O2. In this configuration, a particle in the absolute center of the focal area will affect all beam quadrants to the same extent, but if it is in a distance from this center, corresponding approximately to the diffraction limit of ∼200 nm, its influence on the optical pathway of one beam quadrant is as big as in the configuration shown in Figure 1c.[31] After the

beam splitter, BS, one part of the beam quadrants is running parallelly to the table along BS−QP−M2−Rt1 and back, but the other is reflected vertically at the flat mirror M3 and the roof top mirror Rt2. This provides a relative flip of the electric field vector of the light in the part running along M2 and Rt1. Such an arrangement is necessary for a deep cancellation and also allows nulling of broadband light (up to 200 nm fwhm, for details, see ref 27). Note that, actually, both beam quadrants are running along the two possible interferometric paths BS−QP−M2−Rt1 and BS−M3−Rt2 simultaneously. The beam splitter, therefore, is used in double-pass: each input beam quadrant is modulated by the same beam splitter reflection/transmission product, thus automatically maintaining intensity balance for all wavelengths. The lens, L2 ($f = 5$ cm) is focusing the output beams onto the detector single-mode fiber. This ensures that only the core of the output point-spread function is detected, thus largely eliminating the effect of wave front irregularities.[28]

Material and Experimental Details

Details of the Interferometer. As light source, a fraction of light either from a home-built fs-titan:sapphire oscillator (800 nm, 500 mW, <100 fs pulse width, 90 MHz), a HeNe−Laser beam (632.18 nm, 10 mW, Spindler & Hoyer, Göttingen, Germany), or a white light source (wolfram lamp) was available. Two water immersion objectives were used (Olympus Uapo 40× and Uplaplo 60×, Olympus, Hamburg, Germany). We found no significant differences in the obtained nulling depths using different combinations of microscope objectives. Depending on the light source, about 20−40 μW were sent into the first microscope objective. To accurately steer the collimated

Proteins and Nanoparticles in a Deep Nulling Microscope
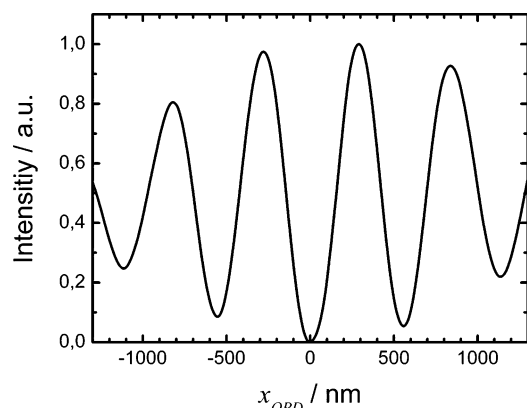
J. Phys. Chem. B, Vol. 109, No. 38, 2005 **18165**

Figure 3. Intensity at the nulled exit as a function of the optical pathway difference, x_{OPD}, measured during a full sweep of the piezoactuator at M2. To find the global null position, spectrally broad light (~600−800 nm) from a filtered Wolfram lamp was used.
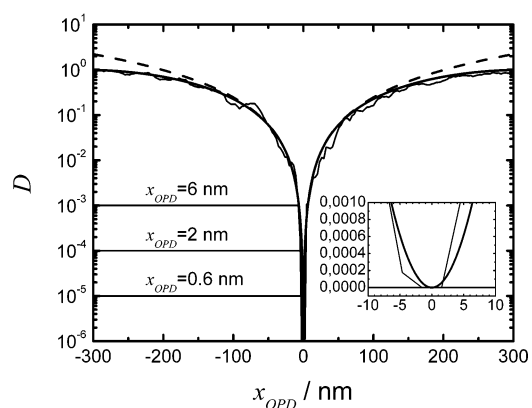

Figure 4. Normalized measured countrate (null depth, D, thin line) at the nulled exit as a function of the optical pathway difference, x_{OPD}, along with theoretical curve (eq 1, exact curve: thick solid line; approximation: dashed line). The inset (linear plot) shows that the transient null corresponded to two subsequent measured values of zero counts. Horizontal lines: necessary level of optical path length accuracy. The sample in the microscope focus was an aqueous buffer solution. $\lambda = 632$ nm.

beam quadrants emerging from the second microscope objective O2 into the detection unit, a 3D piezostage (P611, E664, PI−System, Karlsruhe, Germany) mounted to O1 and the adjustable mirror M1 (AHF Analysentechnik, Tübingen, Germany) were used. The quartz plate, QP, was inserted into the path BS−QP−M2−Rt1 to equalize the amount of glass all beam quadrants were passing. Fine adjustments of the group velocity dispersion were done by slightly tilting QP. To accurately control the optical pathway length in the interferometric path BS−QP−M2−Rt1, the mirror M2 was mounted on a piezotranducer (2 μm travel, S303, E802, PI−System, Karlsruhe, Germany) and a micrometer stage controlled by a picomotor actuator (2.5 cm travel, NF831, NF8753, Newfocus, San Jose, USA). Single photons were counted by either using an avalanche photodiode (AQR-13, Perkin-Elmer, Dumberry, Canada) or a photomultiplier (R1464, Hamamatsu, Hamburg, Germany) connected to a photon counter (SR400, Stanford Research Systems, Sunny Valley, USA). First, a global null position was found for the whole setup using the M2 picomotor actuator and the pulsed laser or the white light source. Then fine adjustments where done with the piezoactuator itself (Figure 3). The controller of the piezocrystal was connected to a home-built minicomputer, which can be programmed with different algorithms to move the piezo actively according to the photons counted at the detector.

The null depths were successively improved by aligning all controls of the interferometer. The whole interferometer was enclosed in a box covered with acoustic insulating foam and placed on an air-damped table. The deepest nulls where achieved by controlling picomotor actuators, steering the angles of M3 and also M2 from outside the box.

Samples. The samples were inserted between the objectives using a home-built flow cell consisting of a sandwich structure of several cover slips. The samples itself were flown in the gap between two cover slips. During measurements, the sample flow was stopped. A PBS buffer (Sigma-Aldrich, D8537) was used as a blank sample. Diluted buffer solutions of 20-, 100-, and 200-nm spheres (Molecular Probes Kit F-8888) were sonicated and centrifuged prior to use. The PS I samples were diluted with a buffer solution containing 20 mM 2-(N-morpholino)-ethanesulfonic acid (MES) at pH 6.5, 20 mM KCl, 20 mM CaCl$_2$, and 0.02% dodecyl-β-D-maltoside (β-DM) and also sonicated and centrifuged prior to use. The preparation of the trimeric PS I itself has been described elsewhere.[30]

Two-Photon Fluorescence Correlational Spectroscopy (2P−FCS). For comparison of the interferometric data with

conventional two-photon fluorescence data of the fluorescing spheres, the setup was modified to comprise a standard confocal microscope setup. For details of such a setup see, e.g., ref 12. Here, we only briefly describe the modifications done to our setup for performing such measurements. The home-built fs-titan:sapphire oscillator was used as a two-photon excitation source. A mirror was inserted into the setup (not shown in Figure 2) to steer the 800-nm excitation light directly into the back aperture of O2. Additionally, a dichroic beam splitter (low pass 700 nm, AHF Analysentechnik, Tübingen, Germany) was inserted between this mirror and O2 to direct the sample fluorescence light collimated with O2 toward a lens and focusing it onto an avalanche photodiode (AQR-13, Perkin-Elmer, Dumberry, Canada). All correlation analyses were done via software correlation.

Results

Transient Nulls and Stabilized Nulls. Our first goal was to achieve nulls with microscope objectives and using an aqueous buffer solution as deep as in the idealized setup used by the astronomers. The transient null depths are best measured by scanning the piezoactuator of M2 linearly over a range corresponding to the global null and the two nearest maxima. In Figure 4, such a scan is shown. It shows that it is possible to achieve transient nulls on the order of about 10^{-5} on a daily basis in aqueous buffer solution. The actually transient null might be even deeper. Determination of the real depth of the transient nulls is difficult because, in the minimum, 0 photons are counted with the optimum parameters for the temporal width of the photon counting time channels during a scan. This would give an unrealistic absolute value of $D = 0$. However, from our data, we can conclude that the nulls must be better than or equal to $5 \cdot 10^{-5}$. These are the best nulls when there is at least one count in one time channel in the minimum. According to eq 1, a null of better than $5 \cdot 10^{-5}$ corresponds to a pathway accuracy of better than 1 nm.

A dithering feedback algorithm can stabilize the interferometer at a position as close as possible at $x_{OPD} = 0$ nm. This stabilization is limited by the vibrational isolation of the system, which is not ideal yet. Nevertheless, the current level of vibrational isolation already allows stabilizing of nulls of about $5 \cdot 10^{-4}$. These stabilized nulls already correspond to a pathway
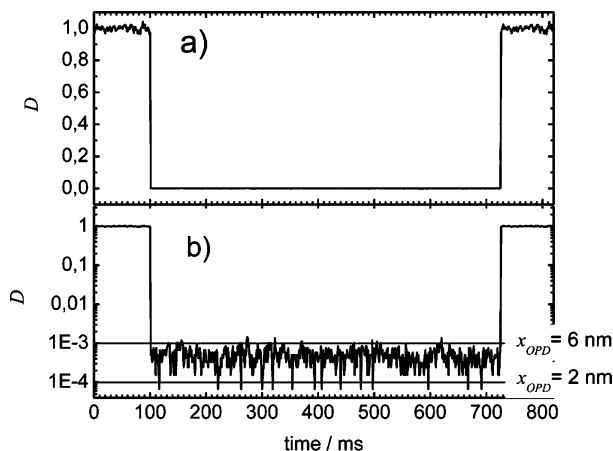
Figure 5. A trace showing the stabilization by the computer at a minimum x_{OPD} corresponding to nulls of about $D \approx 5 \times 10^{-4}$ (100–720 ms) and at $x_{OPD} = \lambda/2$ ($D = 1$, 0–100, and 720–820 ms). (a) Linear plot. (b) Logarithmic plot. Horizontal lines: necessary level of optical path length accuracy. The sample in the microscope focus was an aqueous buffer solution. $\lambda = 632$ nm.
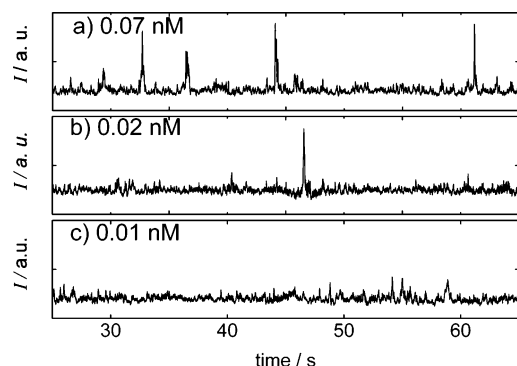

Figure 6. Deep nulling traces of a solution containing 0.07, 0.02, and 0.01 nM 200-nm spheres. The largest spikes are visible when a particle diffuses through the area close to the focus. $\lambda = 632$ nm.

accuracy of about $x_{OPD} \approx 4$ nm (Figure 5). For the correlational analysis of the signals (see below), very similar results can also be obtained without dithering.

Traces of Larger Nanospheres. In our first experiments, we tested the setup with solutions of 100- and 200-nm polystyrene spheres. In Figure 6a–c, deep nulling traces of a 0.07, 0.02, and 0.01 nM aqueous solution of 200-nm polystyrene spheres are shown. Focal transits of individual 200-nm beads can be clearly seen as peaks in the traces. In the most diluted sample (Figure 6c), only minor fluctuations due to single particle transits more remote from the focus were detected during the measuring time. In Figure 7a and b, corresponding deep nulling measurements of ~1 nM 100- and 200-nm polystyrene spheres are shown in comparison with a measurement using pure buffer solution (Figure 7c). One nM corresponds to about 1 bead on average in a focal area that has approximately a diameter of 200 nm and a length of 500–1000 nm. This is a concentration that is well suited for a correlational analysis of the fluctuating signals. The half-width of the peaks in the traces of ~75 ms for 100-nm spheres and ~100–150 ms for 200-nm spheres correspond well with the average diffusional time measured separately via two-photon fluorescence correlation spectroscopy.

Also, the amplitude of the peaks corresponding to an additional optical pathway difference of $x_n \sim 10$ nm for the 200-nm spheres and $x_n \sim 2$ nm for the 100-nm spheres, is
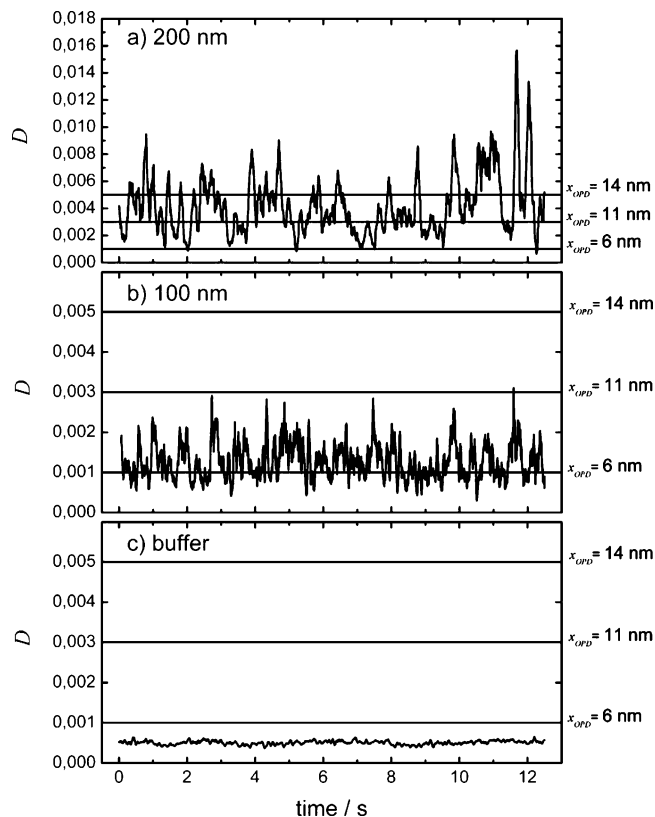

Figure 7. Fluctuational traces of a solution containing ~1 nM 200 nm (a), 100 nm (b) spheres, and (c) of a pure buffer solution. Note that the D axis is displayed linearly in contrast to Figures 4 and 5. 1 nM corresponds to about 1 particle on average in the focal area. $\lambda = 632$ nm.

matching well with the amplitude expected from a simple estimate using the following equation (Figure 7):[32]

$$
x_n = \frac{\int_0^{r_p} W(r) \cdot x_S(r) \cdot \Delta n \cdot r \cdot dr}{\int_0^{\infty} W(r) \cdot r \cdot dr} =
$$

$$
\frac{\int_0^{r_p} e^{-2r^2/r_0^2} \cdot 2 \cdot \sqrt{r_p^2 - r^2} \cdot \Delta n \cdot r \cdot dr}{\int_0^{\infty} e^{-2r^2/r_0^2} \cdot r \cdot dr}. \quad (2)
$$

Here, x_n is the additional optical pathway caused by a particle in the center of the focal region of one interferometer arm, $W(r)$ is the one-dimensional light intensity distribution of this focal region, with r being the radial distance from the optical axis, $x_S(r)$ the optical path length of the light through the particle as a function of r, and $\Delta n = n_p - n_{H_2O} \approx 0.2$ is the difference of the refractive indices of the particle and water. We assumed a Gaussian distribution for $W(r)$, with r_0 being the diameter of the focal region and a spherical function for $x_S(r)$ with a radius of the spheres, r_p. This calculation yields a value of $x_n = 11$ nm for a sphere of $r_p = 100$ nm radius and $x_n = 1.6$ nm for a sphere of $r_p = 50$ nm radius in a focal area of $r_0 = 200$ nm diameter. These values might be surprisingly small, but one has to consider that, for a $r_p = 100$ nm sphere, the maximum change of 40 nm in the optical path length is only obtained along a central axis and that a large amount of light is passing by the sphere (Figure 8). Higher peaks in the traces than the calculated x_n are likely to be due to more than one bead in the detection volume.

Correlational Analysis of Smaller Nanospheres and Biopolymers. The temporal fluctuations of the optical pathway

Proteins and Nanoparticles in a Deep Nulling Microscope

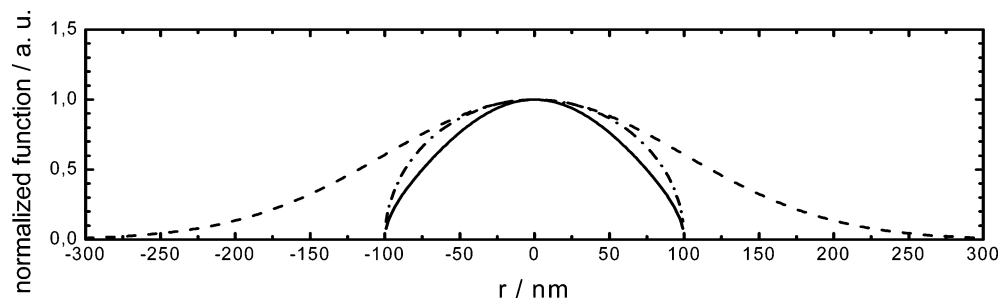*J. Phys. Chem. B, Vol. 109, No. 38, 2005* **18167**

Figure 8. Radial Gaussian intensity distribution $W(r)$ of one focus (dashed line), optical path through a spherical particle $x_s(r)$ (dash dotted line) and resulting convolution $W(r) \cdot x_s(r)$ (solid line). The curves were calculated using $r_0 = 200$ nm and $r_p = 100$ nm. A normalized radial two-dimensional integration of this convolution (eq 2) multiplied by the refractive index change Δn gives the expected maximum optical path length shift, x_n, caused by a sphere in the center of the focal region.

difference $\Delta x_{OPD}(t) = x_{OPD}(t) - \langle x_{OPD}(t) \rangle$ depend on the statistical change in the number of the particles in the focal region, i, and their size. Assuming a Poisson statistic for the particle number, i, $\Delta x_{OPD}(t)$ fluctuates with a standard deviation of $\sqrt{i} \cdot x_n$ (eq 2). For a statistical analysis of the interferometric signals in terms of a temporal correlation function, it is meaningful to correlate the square root of the nulling depth because x_{OPD} is quadratically dependent on D (eq 1):

$$G(\tau) = \langle \Delta x_{OPD}(t) \cdot \Delta x_{OPD}(t + \tau) \rangle \propto$$
$$\langle (\sqrt{D(t)} - \langle \sqrt{D(t)} \rangle) \cdot (\sqrt{D(t + \tau)} - \langle \sqrt{D(t)} \rangle) \rangle \quad (3)$$

$G(\tau)$ is decreasing with increasing τ according to the time for the diffusion of the particles through the focal region. This decrease is comparable to the decrease of fluorescence auto-correlation curves where, usually, the equation $G_f(\tau) = (\langle I(t) \cdot I(t + \tau) \rangle) / \langle I(t) \rangle^2 - 1$ is used. Here $I(t)$ is the fluorescence intensity of fluorescing particles in the focal area measured at the time t. (For details see, e.g., ref 12). An important difference is that the function $G_f(\tau)$ is inversely proportional to the average particle number i and independent from the particle size for small τ, whereas $G(\tau)$ becomes larger for larger particles and also for higher particle concentrations.

Figure 9a shows an autocorrelation curve obtained using eq 3 for the analysis of the data measured with the ~1 nM aqueous solution of 200-nm spheres (dots with solid line as a guide to the eye). In the same plot, a conventional two-photon fluorescence autocorrelation curve from fluorescing 200-nm spheres (dashed line) is also shown. The comparison of both curves yields a good agreement, which shows that the sizes of the focal regions of both methods are similar. The oscillations observed in the deep nulling correlation curves are reproducible. They might indicate cross-correlation terms in the signals due to the close proximity of the beam quadrants in the focal region (Figure 2) or residual vibrations in the setup. A frequency analysis of these oscillations did not result in a single frequency. Thus, further experiments are required to unravel the real nature of these oscillations. Figure 9b shows the corresponding correlation curves of a ~1 nM aqueous solution of 100-nm spheres. Again, good agreement of both correlation curves can be observed. This result shows that deep nulling correlation curves can serve as a label-free method for a diffusional analysis of particles. Figure 9c shows the corresponding correlation curves using a higher concentration of 20-nm spheres. As this is the size of larger biomolecules, such as, e.g., ribosomes, this curve already indicates that it is also possible to perform a label-free correlational analysis of biomolecules in microscopic dimensions. Indeed, Figure 9d shows a corresponding curve of PS I as an example for label-free protein analysis. Trimeric PS I weighs about 350 kDa and has dimensions of about 10−20 nm

including the detergent and hydrodynamic shell. A contribution of chlorophyll absorption around 630 nm to the signals is also possible. We believe that these first data provide an indication that a correlational analysis will also become feasible for smaller proteins and at lower concentrations of the proteins or nanometric spheres once the vibrational isolation of our system allows fully the stabilizing of the transient nulls of 10^{-5} or better. Finally, in Figure 8e, the deep nulling correlation curves of Figure 8a−d are shown without normalization. Clearly, the amplitude of the correlation curves decrease with the particle sizes, even though the concentration of the solutions containing 200- and 100-nm spheres were smaller than the solutions containing the 20-nm spheres and PS I.

Single-Protein Detection Using Coherent Near-Field Sources? In the current microscope setup, the spot size for sensing single diffusional nanoparticle events is limited to about 200 nm by the diffraction of light. This is far bigger than single proteins of a size typically ranging from 1 to 10 nm. However, the spot size can be decreased drastically by using two coherent near-field light sources with diameters on the order of a few tens of nanometers. Recently, we developed a simple technique for the fabrication of such nanoapertures in metallic foils of down to 20 nm diameter (Figure 10, details will be subject of another publication). We inserted the foils containing the nanoholes in the focal region between the microscope objectives and adjusted them three-dimensionally by using a 3D-micrometer stage. First, experiments with the foils basically provided the same nulling curves but with smaller photon counts (Figure 11). This, however, can easily be compensated by a higher incident flux of photons. As each photon emerging from the apertures potentially can be detected at the bright or dark exit of the interferometer, no difficulties with low signal intensities are expected, as they are known from fluorescence applications with nanometric near-field sources. Considering that it is no problem to detect 100-nm spheres in a microscope focus of about 200 nm diameter, we expected that nanometer-sized proteins can be detected in or at 35-nm near-field apertures.

Let us estimate the theoretical signal-to-noise ratio of the expected signals caused by an additional optical pathway shift for the short time of a single particle transit. For a given x_{OPD}, an additional change of the optical pathway difference of x_n results in a change of the detected photons at the dark exit, ΔN, according to:

$$\Delta N = \left| N_0 \cos^2 \frac{x_{OPD} \pi}{\lambda} - N_0 \cos^2 \frac{(x_{OPD} + x_n) \pi}{\lambda} \right| \approx$$
$$N_0 \frac{(2 x_{OPD} x_n + x_n^2) \pi^2}{\lambda^2} \quad (4)$$
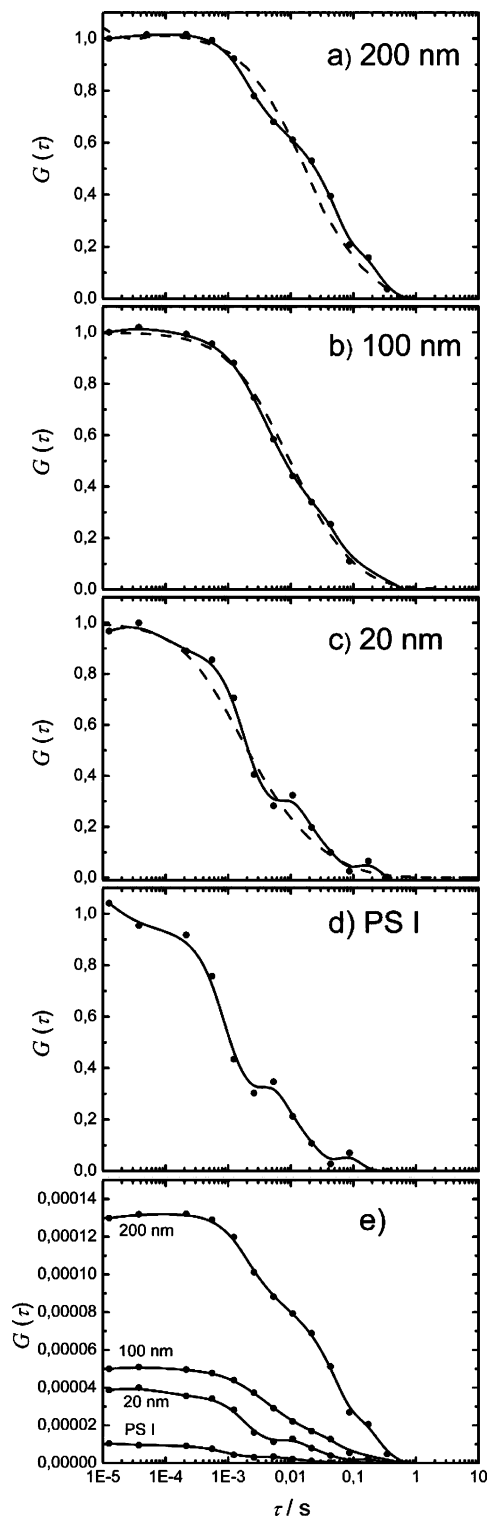
Figure 9. (a) Comparison of a deep nulling correlation curve (line with dots) of an aqueous solution containing ~1 nM 200-nm spheres with a conventional two-photon fluorescence correlation curve of fluorescing 200-nm spheres in the same setup (dashed line). The oscillations in the deep nulling correlation curves are reproducible and might be due to cross-correlation terms or residual vibrations. (b) Corresponding correlation curves of an aqueous solution containing ~1 nM 100-nm spheres. (c) Correlation curves of an aqueous solution of 20-nm spheres. (d) Deep nulling correlation curve of an aqueous solution containing trimeric PS I from *Thermosynechococcus elongatus*. The concentration of the samples (c) and (d) were on the nanomolar scale (>1 nM). All deep nulling curves were measured with a duration of 1 s. The curves shown in (a–d) are normalized to G(0) = 1. In (e), the deep nulling correlation curves from (a–d) are plotted without normalization. $\lambda = 632$ nm.
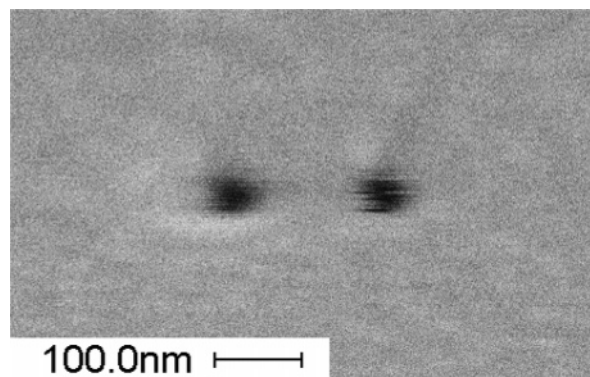

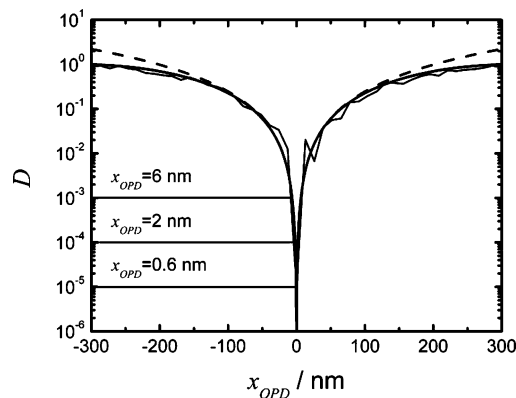**Figure 10.** REM image of two nanoholes of 35 nm diameter.

Figure 11. Normalized measured countrate (null depth, D, thin line) as a function of the optical pathway difference, x_{OPD} using nanoapertures inserted in the focal region of the interferometer. Thick line: theoretical curve (eq 1, approximation: dashed line). For the plot, 30 x_{OPD} scans were added, and the dark count rate of the detector was subtracted. Horizontal lines: necessary level of optical path length accuracy. The sample in the microscope focus was an aqueous buffer solution. $\lambda = 632$ nm.

For the calculation of x_n, we assume that the light intensity distribution at a nanoaperture is also Gaussian and that eq 2 can be used. If the photon noise could be neglected, the highest sensitivity for refractive index changes would not be obtained in the case of an absolutely nulled exit but with an optical pathway difference of $x_{\text{OPD}} = (1 + 2i)\lambda/4$, $i = 0,1,2....$ This is because the slope of N as a function of x_{OPD} is the highest around these x_{OPD} values (eq 3). However, as we are interested in the dynamic behavior of (bio)polymers, the limited maximum photon number during a typical focal transit time of these (bio)-polymers has to be considered. The photon shot noise, σ, for a statistically detected number of photons, N, is $\sigma = \sqrt{N}$. To be able to detect a change in the refractive index during a transit, the change in the detected intensity, ΔN, must be significantly larger than this value. The signal-to-noise ratio is the expected change in the intensity divided by the shot noise of the remaining photons at the dark exit, when the average count rate of remaining photons is regarded as a subtractable offset:

$$\frac{\Delta N}{\sigma} = \frac{N_0 \left| \cos^2\frac{x_{\text{OPD}}\pi}{\lambda} - \cos^2\frac{(x_{\text{OPD}} + x_n)\pi}{\lambda} \right|}{\sqrt{N_0 \cos^2\frac{x_{\text{OPD}}\pi}{\lambda}}} \approx$$

$$\frac{\sqrt{N_0}\,2x_n\pi}{\lambda} + \frac{\sqrt{N_0}\,x_n^2\pi}{x_{\text{OPD}}\lambda} \quad (5)$$

TABLE 1: Calculated Optical Pathway Shifts According to Eq 2 along with Expected Signal-to-Noise Ratios (Eq 5)[a]

focus diameter r_0/nm	particle radius r_p/nm	optical path-length shift per particle x_n/nm	transit time τ_D ms	photons number during a transit N_0	assumed nulling depth D	signal-to-noise ratio $\Delta n/\sigma$
200	100	11	121	1210000	$5 \cdot 10^{-4}$	267
200	50	1.6	75	750000	$5 \cdot 10^{-4}$	16
20	10	2.72	50	50000	$1 \cdot 10^{-5}$	19
20	5	0.55	50	50000	$1 \cdot 10^{-5}$	1.75

[a] For Δn, a value of 0.2 was assumed. The photon number, N_0, sent into the interferometer during a transit through a microscope focus ($r_0 = 200$ nm) of a particle was calculated using the count rate of 10 000 000 s^{-1} detected on the photomultiplier when the interferometer is set to $x_{OPD} = \lambda/4$. The transit time τ_D was derived from conventional fluorescence correlation measurements. For the transit time through a nanoaperture ($r_0 = 20$ nm), we estimated $\tau_D = 50$ ms and used a corresponding count rate of 1 000 000 s^{-1}.
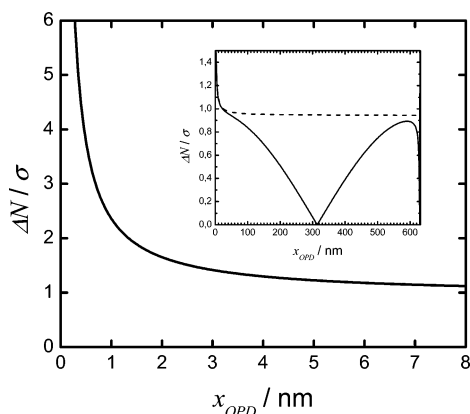

Figure 12. Calculated signal-to-noise ratio as a function of x_{OPD} according to eq 5 (dashed line: approximation). The signal-to-noise ratio becomes significantly greater than one for values of x_{OPD} smaller than 2 nm only. The parameters for the shown curves are $x_n = 3$ nm, $N_0 = 1000$, and $\lambda = 632$ nm.

The signal-to-noise ratio for small x_{OPD} is, therefore, the sum of a term, $\sqrt{N_0}2x_n\pi/\lambda$, which only depends on the incident photon number, N_0, and an additional term, $N_0 x_n^2 \pi/x_{OPD}\lambda$, which increases rapidly with smaller values for x_{OPD}. From this, it follows that, at smaller incident photon numbers, N_0, which can be expected with near-field apertures as light sources, the signal-to-noise ratio is getting increasingly better, the better the interferometer is nulled, i.e., $x_{OPD} = 0$. In Figure 12, the signal-to-noise ratio is shown as a function of the stabilized x_{OPD} for $N_0 = 1000$ photons and a refractive index shift of $x_n = 3$ nm. This corresponds, for example, to a situation where a 20-nm antibody antigene complex is passing by a nanohole and where, during that time, 1000 photons are emerging from this nanohole on average. As can be seen, the signal-to-noise ratio is getting significantly better than one for values of x_{OPD} smaller than 2 nm only.

In Table 1, calculated signal-to-noise ratios for single particle transits are shown as a function of the particle diameter for microscope foci of 200 nm diameter and nanoapertures of 20 nm diameter. From these estimates, it follows that the measured transient nulling depth of $1 \cdot 10^{-5}$ (Figure 4) is sufficient for the detection of a single 5-nm particle diffusing through a 20-nm near-field aperture when, during that time, about 50 000 photons are exiting the near-field apertures.

Outlook and Conclusions

Our results show that it is possible to obtain transient nulls on the order of 10^{-5} in a microscope setup with aqueous solutions corresponding to optical pathway differences of less than 0.6 nm and to actively stabilize the nulls to about $5 \cdot 10^{-4}$. This allows a nonfluorescent fluctuational correlational analysis of trimeric PS I protein complexes of about 10 nm in diameter

and 20 nm polystyrene spheres (Figure 9) and a single particle detection of larger nanospheres (100 nm, 200 nm, Figures 6 and 7) without heating them. The good agreement of the deep nulling correlation curves with conventional two-photon fluorescence correlation curves provides evidence that the detection volume of the label-free method is very similar to detection volume of fluorescence methods (~200 nm in diameter). The amplitudes of the label-free correlation curves provide additional information about the mass of the particles. The method should, therefore, allow a label-free diffusional and size analysis of other biological objects such as vesicles, ribosomes, proteins, and DNA in microscopic dimensions. To gain more specific information about the objects, the exploration of absorption effects (Kramers−Krönig relation) and the combination with nonlinear optical techniques or the optical Kerr effect will be the subject of future studies. The use of a configuration with two slightly tilted arms as shown in Figure 1c might even allow measurements in more complex systems. We are presently exploring the properties of such an arrangement.

Finally, the theoretical considerations (Table 1) provide also strong indication that the setup in combination with the coherent nanometer near-field sources of about 30 nm size (Figures 10 and 11) is potentially even sensitive enough for label-free single biomolecular analysis.

References and Notes

(1) Gryczynski, Z.; Gryczynski, I.; Lakowicz, J. R. *Biophotonics, Part A* **2003**, *360*, 44.
(2) Moerner, W. E.; Orrit, M. *Science* **1999**, *283*, 1670.
(3) Ambrose, W. P.; Goodwin, P. M.; Jett, J. H.; van Orden, A.; Werner, H. J.; Keller, R. A. *Chem. Rev.* **1999**, *99*, 2929.
(4) Deniz, A. A.; Laurence, T. A.; Dahan, M.; Chemla, D. S.; Schultz, P. G.; Weiss, S. *Annu. Rev. Phys. Chem.* **2001**, *52*, 233.
(5) Eigen, M.; Rigler, R. *Proc. Natl. Acad. Sci. U.S.A.* **1994**, *91*, 5740.
(6) Kulzer, F.; Orrit, M. *Annu. Rev. Phys. Chem.* **2004**, *55*, 585.
(7) Kühnemuth, R.; Seidel, C. A. M. *Single Mol.* **2001**, *2*, 251.
(8) Moerner, W. E.; Fromm, D. P. *Rev. Sci. Instrum.* **2003**, *74*, 3597.
(9) Xie, X. S.; Trautmann, J. K. *Annu. Rev. Phys. Chem.* **1998**, *49*, 441.

(10) Noji, H. Y. R.; Yoshida, M.; Kinosita, K. *Nature* **1997**, *386*, 299.

(11) Yildiz A.; Forkey, J. N.; McKinney S. A.; Ha, T.; Goldman, Y. E.; Selvin, P. R. *Science* **2003**, *300*, 2061.

(12) Schwille, P. In *Fluorescence Correlation Spectroscopy: Theory and Applications*; Springer Series in Chemical Physics; Springer-Verlag: New York, 2001, p 360.

(13) Eigen, M.; Rigler, R. *Proc. Natl. Acad. Sci. U.S.A.* **1994**, *91*, 5740.

(14) Walla, P. J.; Jelezko, F.; Tamarat, P.; Lounis, B.; Orrit, M. *Chem. Phys.* **1998**, *233*, 117.

(15) Hess, S. T., Huang S.; Heikal, A. A.; Webb, W. W. *Biochemistry* **2002**, *41*, 697.

(16) Eggeling, C.; Fries, J. R.; Brand, L.; Gunther, R.; Seidel, C. A. M. *Proc. Natl. Acad. Sci. U.S.A.* **1998**, *95*, 1556.

(17) Liedberg, B.; Nylander, C.; Lundstrom, I. *Sens. Actuators* **1983**, *4*, 299.

(18) Kasper, M.; Busche, S.; Dieterle, F.; Belge, G.; Gauglitz, G. *Meas. Sci. Technol.* **2004**, *15*, 540.

(19) Volkmer, A. *J. Phys. D: Appl. Phys.* **2005**, *38*, R59.

(20) Zumbusch, A.; Holtom, G. R.; Xie, X. S. *Phys. Rev. Lett.* **1999**, *82*, 4142.

(21) Mawatari, K.; Kitamori, T.; Sawada, T. *Anal. Chem.* **1998**, *70*, 5037.

(22) Berciaud, S.; Cognet, L.; Blab, G. A.; Lounis, B. *Phys. Rev. Lett.* **2004**, *9325*, 7402.

(23) Boyer, D.; Tamarat, P.; Maali, A.; Lounis, B.; Orrit, M. *Science* **2002**, *297*, 1160.

(24) Cognet, L.; Tardin, C.; Boyer, D.; Choquet, D.; Tamarat, P.; Lounis, B. *Proc. Natl. Acad. Sci. U.S.A.* **2003**, *100*, 11350.

(25) Kwiat, P.; Weinfurter, H.; Herzog, T.; Zeilinger, A.; Kasevich, M. A. *Phys. Rev. Lett.* **1995**, *74*, 4763.

(26) Kwiat, P. G.; White, A. G.; Mitchell, J. R.; Nairz, O.; Weihs, G.; Weinfurter, H.; Zeilinger, A. *Phys. Revi. Lett.* **1999**, *83*, 4725.

(27) Wallace, K.; Hardy, G.; Serabyn, E. *Nature* **2000**, *406*, 700.

(28) Serabyn, E.; Wallace, J. K.; Hardy, G. J.; Schmidtlin, E. G. H.; Nguyen, H. T. *Appl. Opt.* **1999**, *38*, 7128.

(29) Serabyn, E.; Colavita, M. M. *Appl. Opt.* **2001**, *40*, 1668.

(30) Fromme, P.; Witt, H. T. *Biochim. Biophys. Acta* **1998**, *1365*, 175.

(31) The most sensitive region of a beam quadrant with respect to refractive index changes is very close to the focus of the microscope objectives. This is the region where the beam quadrants just can be optically separated, considering the diffraction limit of about 200 nm. The region is determined by a complicated three-dimensional optical transfer function defined by the numerical apertures of the objectives and the position of the detection fiber. In total, eight such regions are present for each of the four beam quadrants, one in front of and one after the focus.

(32) For the calculation, we assumed that the focal region of one interferometer arm has a rotational symmetry around the optical axis. We regard the focal region of one interferometer arm as a binary mixture of the buffer solution with a refractive index of $n_{H_2O} = 1.33$ and the nanoparticles or proteins with a refractive index of $n_p \approx 1.5$. The refractive index of the binary mixture, n_M, can be approximated by the linear dependence $n_M = \Phi_{H_2O} n_{H_2O} + \Phi_p n_p$, where Φ_{H_2O} and Φ_p are volume fractions of the two compounds. In addition, we assume that the light intensity distribution $W(r)$ is invariant along the optical axis of an arm for dimensions smaller than the radius of the particles r_p. To calculate the additional optical path length x_n caused by the sphere, we integrate in eq 2 the additional optical path length $x_S(r)$ weighed by the light intensity $W(r)$. The additional factor r in the integration accounts for the rotational symmetry around the optical axis. The calculated value using this formula is the maximum additional optical path x_n shift one can expect with two clearly separated foci for each interferometer arm. Apparently, the experimental x_n values observed with the current apparatus are very close to the values calculated for two clearly separated foci with a diameter of about $r_0 = 200$ nm. Note that this calculation neglects effects due to absorption or scattering.